RSC Advances

ROYAL SOCIETY OF CHEMISTRY

www.rsc.org/advances

Table of Content

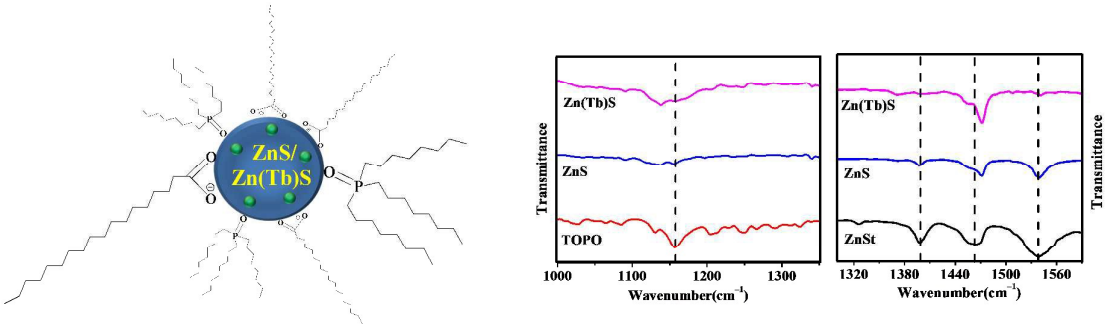

Lanthanide cations tune infrared absorption characteristics of the capping ligands in the Zn(Ln)S [Ln = Sm, Eu, Tb, Dy] nanoparticles.

Lanthanide Cation Induced Tuning of Surface Capping Properties in Zinc Sulfide Nanoparticles: An Infrared Absorption Study

Ankita Ghatak,[1,#] Gouranga H. Debnath,[1] Madhuri Mandal,[2] and Prasun Mukherjee[1,*]

[1] Centre for Research in Nanoscience and Nanotechnology, University of Calcutta, JD-2, Sector-III, Saltlake City, Kolkata-700098, West Bengal, India, E-mail: pmukherjee12@gmail.com

[2] S. N. Bose National Centre for Basic Sciences, JD Block, Sector-III, Saltlake City, Kolkata-700098, West Bengal, India

[#] Present Address: S. N. Bose National Centre for Basic Sciences, JD Block, Sector-III, Saltlake City, Kolkata-700098, West Bengal, India

* To whom correspondence should be addressed.

Abstract

This study reveals the tuning of vibrational characteristics of the capping ligands in the lanthanide [Ln=Sm, Eu, Tb, Dy] cation incorporated zinc sulfide nanoparticles, Zn(Ln)S, as monitored by Fourier transform infrared (FTIR) spectroscopy. Both the stearate and trioctylphosphine oxide (TOPO) were found to be acting as the surface capping ligands for the nanoparticles with multiple co-ordination environments. The vibrational characteristics of the capping ligands in the undoped ZnS nanoparticles exhibited noticeable difference in absorption as compared to that in the pure zinc stearate and TOPO molecules. Lanthanide cation incorporation tunes the corresponding vibrational characteristics to a significant extent, as compared to that in the undoped ZnS nanoparticles. It has been argued that the observed tuning of the capping ligand IR absorption characteristics has been induced by the lanthanide cations that are located near or on the surface of the nanoparticles. The IR spectra suggest a

probable change of carboxylate co-ordination environment in the Zn(Ln)S nanoparticles. The results obtained from the ZnS based nanoparticles were analyzed based on a semi-quantitative analysis and compared with that in the ZnSe and Zn(Tb)Se nanoparticles, in order to evaluate the effect of the constituent anion of the nanoparticles in modulating the IR signature.

Keywords

Zinc sulfide nanoparticles, surface capping ligand, trivalent lanthanide, Fourier transform infrared (FTIR) spectroscopy.

Introduction

The luminescence of trivalent lanthanide cation (Ln^{3+}) that originates from the intra-configurational 4f-4f transitions is unique due to the sharp emission bands, longer lifetime (microseconds to milliseconds time domain), minimum inter-lanthanide spectral band overlap and resistance to photobleaching. [1-11] These properties make the lanthanide based materials attractive in biological imaging, bio-analytical and sensing applications,optoelectronics and telecommunications. [3, 12] The luminescence of Ln^{3+} spans over the entire visible and near infrared (NIR) spectral regime. A NIR probe has advantages in biological imaging applications due to deeper penetration in tissues.

In order to realize the lanthanide luminescence for practical applications, some significant challenges need to be addressed. First, the molar extinction co-efficient of Ln^{3+} is extremely low [13] ($\leq$10 $M^{-1}cm^{-1}$ as compared to 10^4-10^5 $M^{-1}cm^{-1}$ for typical organic fluorophores), resulting direct optical excitation of Ln^{3+} cations to its excited state difficult. Second, the Ln^{3+} luminescence is effectively quenched by the vibrational overtone of –OH, –NH, –CH bonds, [14] necessitating an optimum Ln^{3+} co-ordination environment that protects the cations from both ligand and solvent vibrations. A way to overcome these challenges can

be realized by incorporating Ln^{3+} cations in semiconductor nanoparticle matrix, where the nanoparticles act as an optical antenna and protective matrix for Ln^{3+} luminescence. [15-20] In addition to this, the lanthanide incorporated semiconductor nanoparticles offer other important properties that are otherwise directly not accessible in lanthanide based molecular organic complexes; first, inclusion of multiple Ln^{3+} cations in a nanoparticle resulting the particle brighter and second, formation of multiplex assays, that is, obtaining multiple and distinct emissions by exciting the nanoparticle at a given wavelength. [21, 22]

Despite various efforts, there is a significant controversy in ascertaining the spatial location of Ln^{3+} cations inside the nanoparticles (core versus surface). For example, Bol and co-workers [23] argued that the size and charge mismatch of Ln^{3+} and the constituent cations of II-VI semiconductor materials poses restriction in doping the lanthanide cations in these materials. However, previous works by one of these authors and various other researchers have reported experimental evidence supporting lanthanide incorporation in II-VI semiconductor nanoparticles. [15, 16, 18-20, 24-27] Although these studies point to the fact that it is possible to incorporate lanthanide cations in the semiconductor nanoparticles under appropriate synthetic conditions, they do not clearly identify the core and surface localized Ln^{3+} in the nanoparticles. For example, the Tb^{3+} and Eu^{3+} luminescence in the ZnS nanoparticles were found to be bi-exponential with a shorter sub-milliseconds and a longer lifetime component with few milliseconds duration, [16, 28] where the origin of the two lifetime components were explained to likely originate from two sub-populations of Ln^{3+} in the nanoparticle. That is, the surface localized lanthanides being more exposed to the solvent could originate the shorter lifetime component, whereas the corresponding core localized cations being well protected from the environmental effects originate the few millisecond lived lifetime component. In a recent study by one of these authors, a comparison has been made between the synthetically incorporated Tb^{3+} and Eu^{3+} in the ZnS nanoparticle and the

corresponding post-synthetically treated systems. [28] It is to be noted that a cation exchange reaction in semiconductor nanoparticles is possible by post-synthetic modification of nanoparticles. [29-34] A comparison of Eu^{3+} asymmetry ratio, luminescence lifetime and luminescence lifetime distribution revealed a distinct difference between the two Eu^{3+} incorporation strategies in the ZnS nanoparticles with a more surface related Eu^{3+} contribution in the post-synthetically treated sample compared to that in the synthetically incorporated system. [28] A mixture of population of Ln^{3+} may co-exist in the core and surface of the nanoparticles; depending on the synthetic condition of nanoparticles, concentration of dopants, among other factors. These studies clearly point to the fact that it is important to understand the surface capping properties of the lanthanide incorporated nanoparticles in order to evaluate any effect on the ligand characteristics in presence of lanthanides. This study aims to understand the surface chemistry of the undoped ZnS nanoparticles and the possible tuning of the properties in presence of lanthanide cations by Fourier transform infrared (FTIR) spectroscopy.

FTIR spectroscopy is a unique tool for structural characterization and has been used to characterize the nanomaterials. [35-48] Efrima and co-workers [36] have studied the capping of silver nanoparticles by various long chain carboxylates and for the stearate system, identifying a shift of 44-100 cm^{-1} for the carboxylate stretching frequency in the nanoparticle compared to that in the silver salt. Herman and co-workers [38] characterized the ligand exchange reaction between TOPO and pyridine in the CdSe nanoparticles. The surface composition of the YPO_4 nanoparticles capped with oleate and 2-theonyltrifluoroacetone has been studied by Lin and co-workers. [39] Lis and co-workers [40] have identified glycerine as the capping ligand in the Tb^{3+} doped fluoride nanocrystals. The ligand exchange reaction between either the oleate or TOPO capped CdS nanoparticles and thiol containing ligands have been investigated by McQuillan and co-workers. [41] A spectral band shift has been

observed by Nocchetti and co-workers in Eu and Yb doped ZnAl layered double hydroxides, compared to that in the corresponding undoped counterpart. [43] Although various researchers have characterized the capping of the nanoparticles of varying sizes by IR spectroscopy and discussed the usefulness of studying the IR absorption in the nanometer sized particles, only few studies address any possible dopant induced tuning of ligand characteristics in the doped nanoparticles.

Our study is organized as follows. The synthesized nanoparticles were first characterized by transmission electron microscopy (TEM), energy dispersive X-ray (EDX) spectroscopy and electronic absorption spectroscopy. The surface capping properties of the materials were studied by Fourier transform infrared (FTIR) spectroscopy in order to first identify the capping ligands on the nanoparticles. Then a study has been performed on the possibility of tuning the surface capping properties between the undoped and lanthanide (Sm^{3+}, Eu^{3+}, Tb^{3+}, Dy^{3+}) incorporated ZnS nanoparticles. These systems were considered as representative cases and multiple lanthanide cations were used to verify the generality of the IR spectroscopic properties. The effect of constituent anion of the nanoparticle has been evaluated by performing experiments with the ZnSe and Zn(Tb)Se nanoparticles. The role of possible intercalation of Ln^{3+} in the hydrocarbon chain of the capping ligands, an evaluation of the spatial location of the lanthanide cations in the nanoparticles and the possible contribution from lanthanide stearate salts in modulating the observed IR signals have been evaluated.

Materials and Methods

Chemicals. Trioctylphosphine (TOP) (90%), trioctylphosphine oxide (TOPO) (90%), zinc stearate (ZnSt) (tech.), tetracosane (99%), octadecene (90%) (tech.) and stearic acid (SA) (95%) were purchased from Sigma-Aldrich. Chloroform and methanol were purchased from

Merck. Sulfur (99.999%) was purchased from Fisher Scientific. Terbium (III) nitrate (99.9%), europium (III) nitrate (99.99%), samarium (III) nitrate (99.9%) and dysprosium (III) nitrate (99.9%), selenium powder (99.999%) and tetramethylammonium hydroxide hydrate (TMAH) (90%) were purchased from Alfa Aesar. In all cases, hydrated lanthanide salts were used. Potassium bromide (KBr) IR grade was purchased from Sigma-Aldrich. Argon gas was purchased from Hindustan Gases and Welding. All chemicals were used as purchased without additional purification.

Nanoparticle Synthesis. The ZnS nanoparticles were synthesized based on a report by Peng and co-workers [49] and later modified by Waldeck, Petoud and co-workers. [16, 28] Specifically, a solvent system consisting of octadecene and tetracosane was utilized for the synthesis of the ZnS nanoparticle systems. The cation and anion precursors are zinc stearate, lanthanide nitrate salts and sulfur respectively. Tetracosane (2.0 g), octadecene (3.0 ml), TOPO (1.7 g), and 0.68 mmol of zinc stearate were loaded into a 25 ml three neck, round-bottom flask and refluxed at 300 °C while stirring under argon. After heating this mixture, the lanthanide stock solution (0.12 mmol lanthanide nitrate dispersed in 3 ml trioctylphosphine, this step requires sonication) was injected and allowed to stir within the reaction mixture. The sulfur stock solution (0.40 mmol sulfur powder dissolved in 2.5 ml octadecene with sonication) was injected approximately one hour after the lanthanide stock solution injection. After 20 minutes of growth, the reaction was stopped by removal of the heat source. The nanoparticles were made to precipitate by adding methanol to a chloroform solution (in approximately 5:1 volume/volume solvent ratio) of the synthesized materials. The materials were isolated by centrifugation. The purification steps have been repeated two times for all the nanoparticles studied. The resulting nanoparticles (in which the presence of the precursors were not evident, as judged by the IR absorption bands; *vide infra*) were used for all the measurements performed in this study. Undoped (not incorporating lanthanides) ZnS

nanoparticles were prepared using the methods described above, with the lanthanide precursor addition omitted.

For ZnSe based nanoparticles synthesis, a similar protocol has been adopted as described above, with the replacement of sulfur by selenium as the anionic precursor for the nanoparticles.

Lanthanide (III) Stearate Synthesis. Lanthanide (III) Stearate synthesis was performed based on a report by Peng and co-workers. [50] Specifically, 10 mmol of stearic acid (SA) was dissolved in 20 ml methanol and this mixture was heated to 50-60°C under stirring condition until it became a clear solution. This solution was then allowed to cool to room temperature. A separate solution of tetramethylammonium hydroxide (TMAH) was prepared by adding 10 mmol TMAH in 6.3 ml methanol and was subsequently added to the SA solution. The mixture was stirred for 20 minutes to ensure completion of the reaction. Ln (III) nitrate (Ln=Sm, Dy) solution was prepared separately by dissolving 5 mmol of the nitrate salt in 6.3 ml methanol. This solution was then added drop-wise to the solution containing SA and TMAH under stirring. A white precipitate appeared and it was separated by filtration using a Whatman 1 filter paper. The precipitate was repeatedly washed with methanol and dried before the spectroscopic characterizations were performed.

Electron Microscopy Measurements. The morphology of the nanoparticles were characterized by transmission electron microscope (TEM) [Model: JEOL, JEM-2100] operated with an acceleration potential of 200 kV. HRTEM micrographs and EDX spectrum were obtained for the Zn(Tb)S nanoparticles. The images were processed with Digital Micrograph 2.3 software. TEM samples were prepared by placing a drop of colloidal solution (obtained by dispersing a very small amount of nanoparticles in chloroform) on carbon-coated copper grids and removing the extra solution by drying the grid for ~18 hours.

Fourier Transform Infrared Spectroscopy. Fourier transform infrared spectra were obtained with a Jasco FTIR 6300 spectrometer. The spectra presented were obtained from an average of 64 scans. The resolution of the spectra was 4 cm^{-1}. Samples were prepared using a KBr pellet. Typically ~1 mg of the sample was mixed with ~100 mg of dried KBr in a mortar and pestle. The KBr pellet was prepared by the application of pressure. The spectra were acquired at room temperature. All data analysis was performed with the data analysis software provided with the FTIR instrument.

Stern-Volmer Quenching Experiments. A known amount of the Zn(Tb)S nanoparticles was dissolved in chloroform. This stock solution was divided in seven parts. To these solutions, 0, 20, 50, 100, 200, 300 and 400 µl methanol was added. The emission spectra were collected exciting the samples at 280 nm and the nanoparticle emission subtracted intensities at ~545 nm ($^5D_4 \rightarrow {}^7F_5$) were used to construct the Stern-Volmer plot. For the calculations, first the spectral region from 520 nm to 570 nm has been interpolated by two data points, which was then interpolated with a 1 nm resolution. This contribution from the nanoparticle emission at these wavelengths was then subtracted from the experimentally acquired emission spectrum of Zn(Tb)S nanoparticles, resulting the contribution from Tb^{3+} luminescence at these wavelengths without the contribution from the nanoparticle broad emission. All intensity values were corrected for the absorbance at the excitation wavelength. The Tb^{3+} has been considered as a representative case and the choice was entirely based on the prominent lanthanide band centered luminescence in the Zn(Tb)S nanoparticles, that has been reported previously. [16, 28] All luminescence spectra were acquired in the Horiba Jobin Yvon Fluorolog 3 spectrometer and were collected at room temperature. The excitation and emission slits were set at 4 nm for the acquisition of the spectra. A long pass filter was used to remove the harmonic peak of the excitation light.

Results and Discussion

General Characterization of Nanoparticles. The morphology and structural analysis of the Zn(Tb)S nanoparticles were studied with the results obtained from TEM. Figure 1(a) displays the TEM image of large number of assembled Zn(Tb)S nanoparticles. It can be observed that the particles are of spherical shape with its size in the range of 2.4 ± 0.4 nm in diameter (Figure 1b). The HRTEM image in Figures 1(c) and 1(d) shows the ZnS nanoparticles are crystalline. The planar spacing of about 0.29 nm and 0.19 nm are shown in Figures 1(c) and 1(d) respectively corresponds to the spacing for (101) planes and (110) planes of ZnS hexagonal structure reported in the database of Joint Committee on Powder Diffraction Standards (JCPDS) (Card 36-1450). Figure 1(e) shows the energy dispersive X-ray (EDX) spectrum of the Zn(Tb)S nanoparticles. The EDX spectrum (Figure 2e) shows the presence of terbium in the nanoparticles. The presence of copper in the EDX spectrum most likely originates from the carbon coated-copper grid.

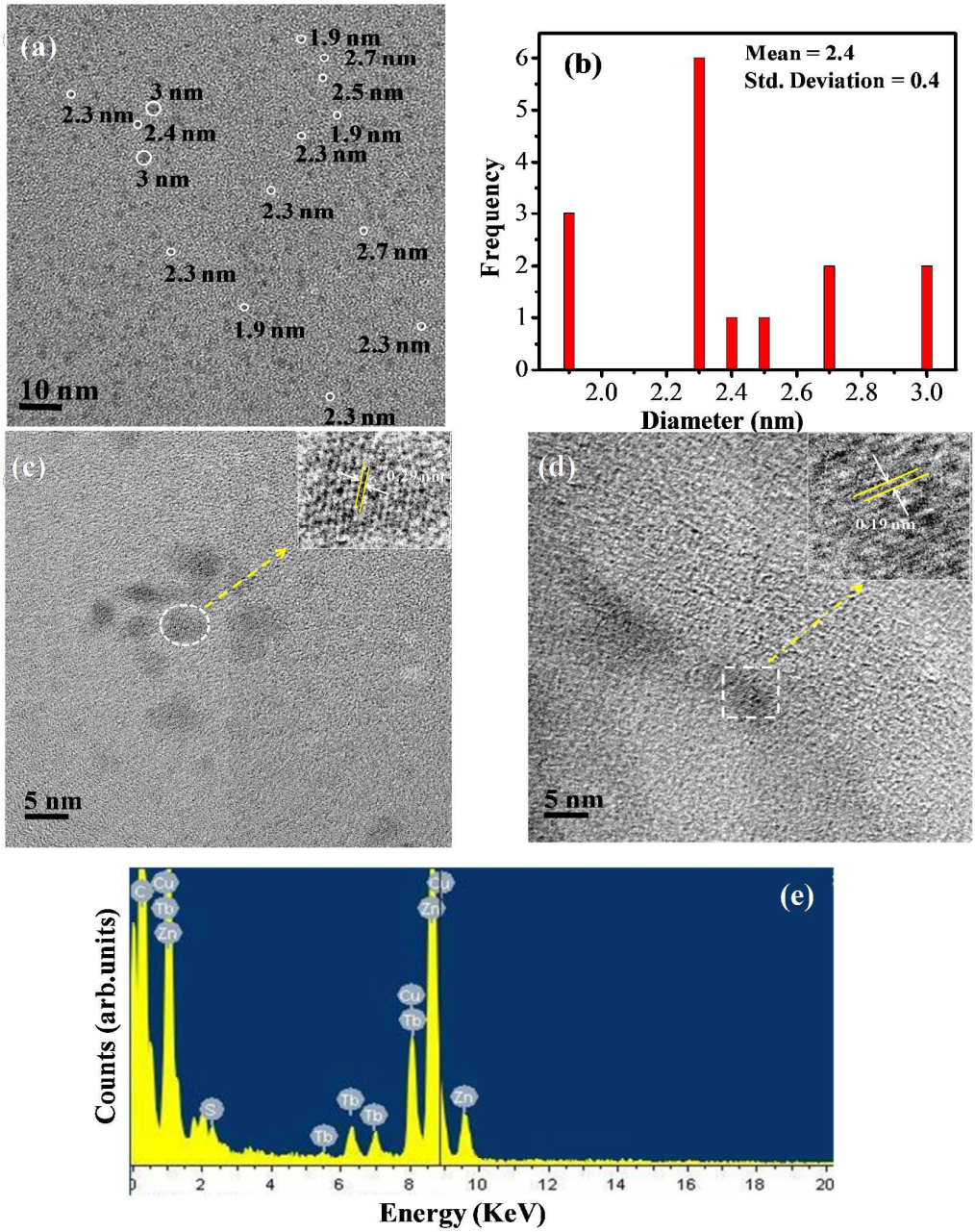

Figure 1. HRTEM micrographs of the Zn(Tb)S nanoparticles: (a) low magnification micrograph showing uniform spherical particle size distribution (b) particle size distribution as obtained from Image J software (c) and (d) showing high magnification images of particles with inset showing their crystal lattice spacing 0.29 nm and 0.19 nm respectively (e) the EDX spectrum. The EDX spectrum shows the presence of terbium in the nanoparticles.

Representative absorption spectra of ZnS and Zn(Ln)S [Ln=Tb, Eu] nanoparticles are shown in Figure 2. The position of the lowest excitonic band maximum has been unaffected by the incorporation of lanthanide cations in the ZnS nanoparticles studied. The band centred at ~287 nm has been assigned to the band gap transition. An estimation of size of the nanoparticles with the help of equation 1, that is based on an empirical relationship proposed by Brus, [51] yields a value of 3.0 nm diameter.

$$\Delta E \approx \frac{\hbar^2 \pi^2}{2R^2}\left[\frac{1}{m_e}+\frac{1}{m_h}\right]-\frac{1.8e^2}{\varepsilon R} \quad (1)$$

where ΔE, R, m_e, m_h, ε are the increment of band gap in the nanoparticles compared to that in the bulk material, radius of the nanoparticles, effective electron mass, effective hole mass and dielectric constant of the host material respectively. The values of effective masses and dielectric constant were taken from a study by Murphy and co-workers. [52] A comparison of the nanoparticle diameter obtained from the TEM measurements reveal that the Brus model slightly overestimates the diameter in this size range. An estimation of size based on an empirical relationship proposed under tight binding model [53, 54] following equation 2 results a value of 2.3 nm for the diameter of the nanoparticles. This estimation is in reasonable agreement with the size distribution obtained from the TEM measurement.

$$\Delta E = \frac{1}{ad^2+bd+c} \quad (2)$$

where ΔE and d are the increment of band gap in the nanoparticles compared to that in the bulk material and diameter of the nanoparticles. The values of a, b and c for ZnS has been considered as 0.2349 $nm^{-2}eV^{-1}$, –0.0418 $nm^{-1}eV^{-1}$ and 0.2562 eV^{-1} respectively and adopted from the study by Sarma and co-workers. [54] The non-zero absorbance contribution at relatively longer wavelengths in the absorption spectra most likely originates from surface

trap states of the nanoparticles. At this point, this is to note that the absorption spectra reported in the Figure 2 have been collected with an absorbance of ~0.2 at 300 nm. In order to evaluate the possible role of scattering in the longer wavelength region in the spectra shown in Figure 2, the samples were systematically diluted to approximately five times and the corresponding absorption spectra were recorded. The non-zero absorption contribution at the longer wavelength region in the absorption spectra was evident in all the diluted nanoparticle samples studied. This corroborates with the assignment that this band primarily originates from the various surface states of the nanoparticles and the contribution from scattering has negligible effect (assuming a linear contribution, a simple analysis by comparing the normalized absorption spectra obtained with various dilutions indicate a scattering contribution of <10% at around 500 nm) in the spectra shown in Figure 2.

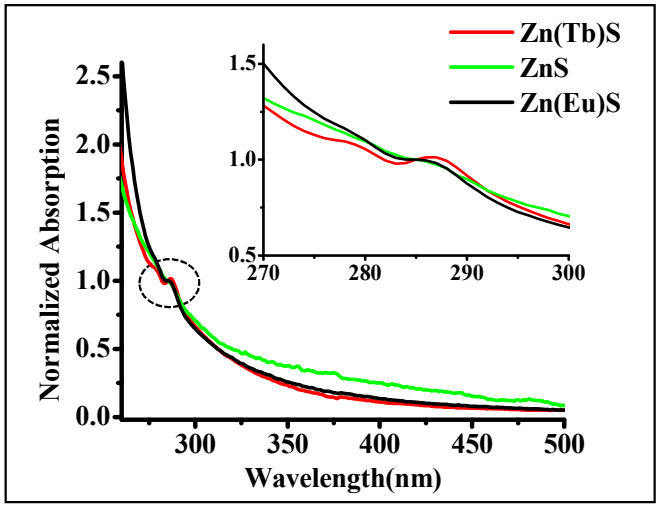

Figure 2. Representative absorption spectra of ZnS, Zn(Tb)S and Zn(Eu)S nanoparticles are shown. The band centred at ~287 nm has been assigned to the band gap transition.

The general synthetic protocol and the doping percentage used to prepare the Zn(Ln)S [Ln=Sm, Eu, Tb, Dy] nanoparticles in the present study has been adopted from previous studies by one of these authors. [16, 28] Based on the steady-state, time-gated and time-resolved luminescence spectroscopy of the Zn(Ln)S [Ln=Eu, Tb] nanoparticles and a series of control experiments, it has been argued that this synthetic protocol can be used to incorporate the

Ln^{3+} cations in the ZnS based nanoparticle matrix. This argument was based on the following observations. First, upon monitoring the lanthanide band centered luminescence, the excitation spectra reveal a relatively structure-less profile that differs significantly from the corresponding spectra in the Ln(III) nitrate dissolved in bulk solvent, where the excitation spectra have been dominated by the sharp intra-configurational 4f-4f bands. This argues in favor of an optical antenna effect operating involving the electronic structure of the nanoparticles in order to sensitize the Ln^{3+} luminescence in the Zn(Ln)S nanoparticles. Second, the lanthanide band centered luminescence lifetime and the lifetime distribution analysis give a millisecond lived component in the Zn(Ln)S [Ln=Eu, Tb] nanoparticles, indicating a well protected Ln^{3+} environment in the nanoparticles. The observation of the optical antenna effect and the longer lifetime component in the luminescence experiments collectively argue towards the incorporation of the Ln^{3+} cations in the Zn(Ln)S nanoparticle matrix by means of the synthetic protocol used in the present study.

The nanoparticle diameter of ~2.4 nm indicates the importance of surface atoms in determining the properties of the nanoparticles.

Fourier Transform Infrared (FTIR) Spectroscopy. Table I summarizes the characteristic IR peak frequencies obtained from the different systems studied. The corresponding IR spectra are shown in figure 3. An enlarged view of selected IR bands is shown in figure 4. The tabulation of peak frequencies in table I was performed considering the spectra in three spectral regions, namely the relatively higher (3000-2800 cm^{-1}), medium (1600-1200 cm^{-1} and ~1150 cm^{-1}) and lower (1000-700 cm^{-1}) frequency domains. The spectral regions have been chosen considering the characteristic absorption by specific functional groups in these ranges. An assignment of representative peak frequencies in table I have also been made.

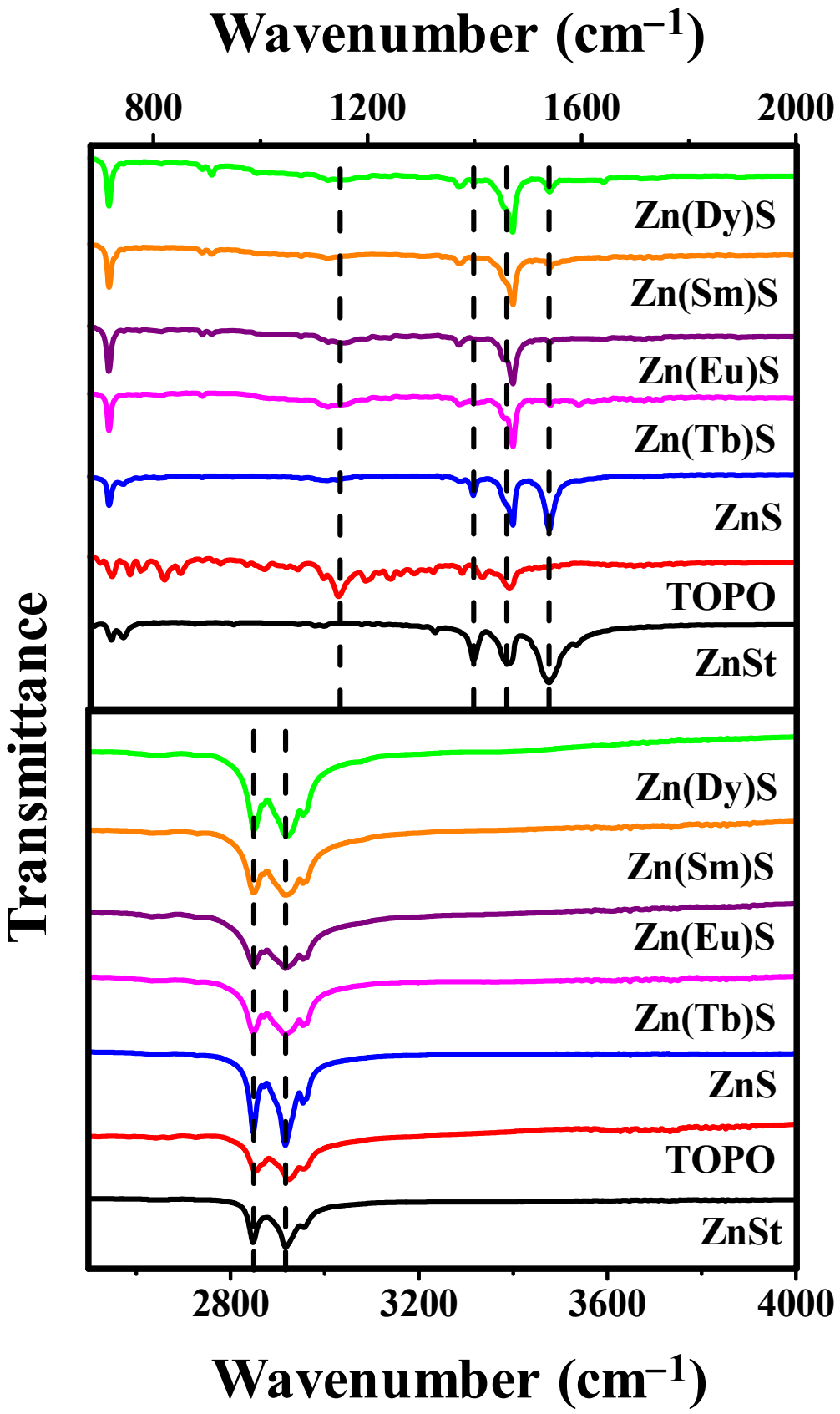

Figure 3. Representative FTIR spectra of the different systems studied. The spectra of the nanoparticles indicate both stearate and TOPO as the capping ligand.

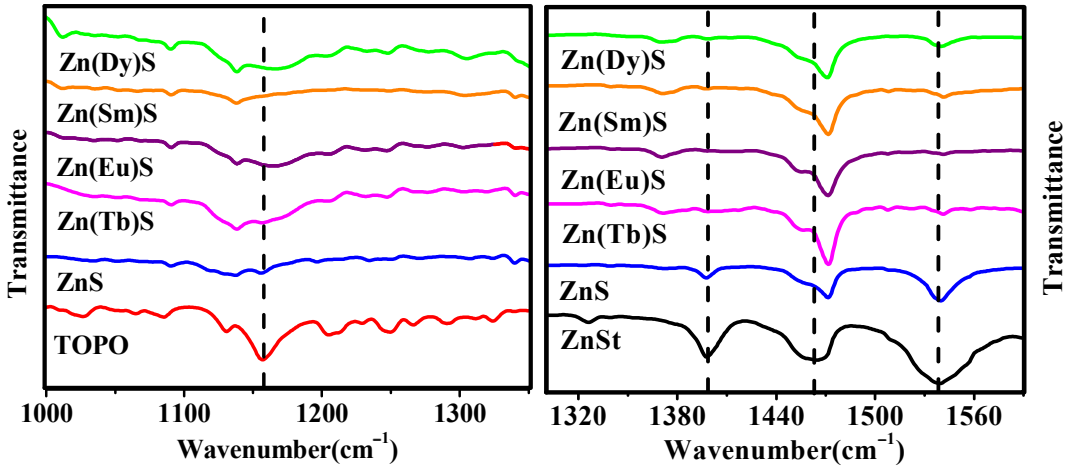

Figure 4. An enlarged view of the FTIR spectra in the P=O (left panel) and the $-COO^-$ (right panel) stretching band regions respectively in the different systems studied is shown. The spectra of the nanoparticles indicate a modification in the characteristics of the capping ligand moiety as compared to that in the pure zinc stearate and TOPO.

Zinc Stearate. In zinc stearate (ZnSt), characteristic IR peaks appear at 2954, 2916, 2872 and 2848 cm^{-1} from the alkyl chain. These bands have been assigned to the asymmetric and symmetric stretching vibrations of the $-CH_3$ and $-CH_2$ groups (Table I). The spectral region of ~1400-1550 cm^{-1} shows multiple peaks. The peaks at 1538 and 1396 cm^{-1} have been assigned to the asymmetric and symmetric stretching vibrations of $-COO^-$ group respectively, whereas the band at 1464 cm^{-1} has been assigned to the in-plane deformation of the $-CH_2$ group. At relatively lower energy range, the peak at 720 cm^{-1} has been assigned to the out-of-plane deformation of the $-CH_2$ group. The peak positions were found to be in agreement with the study by Kojima and co-workers [55] for the zinc stearate.

At least two spectral regions in ZnSt require discussion. First, the peak frequencies in between 2840-2960 cm^{-1} that originates from the long chain alkyl moiety. Various researchers have devoted considerable attention in characterizing this signature. [56-58] Snyder

and co-workers [57] have demonstrated that the IR peaks are shifted to higher energy by at least 6 cm^{-1} in the disordered liquid state compared to that in the ordered crystalline state. Specifically, while in the crystalline state the IR bands appear at 2920 and 2850 cm^{-1}, they appear at 2928 and 2856 cm^{-1} respectively in the corresponding liquid state. The peak positions observed in ZnSt argues in favour of a crystalline ordered state. Second, the spectral region consisting of asymmetric and symmetric stretching bands of the $–COO^-$ group. A correlation has been sought between the difference of asymmetric and symmetric stretching peak frequencies Δ (where $\Delta = \nu_{as}\ [COO^-] - \nu_s\ [COO^-]$) and the nature of carboxylate co-ordination environment. [59-64] Major carboxylate co-ordination structures are summarized in Figure 5. While a larger value of Δ indicates a uni-dentate co-ordination, relatively smaller values indicate a chelating and bridging bi-dentate arrangement. In ZnSt, the Δ value of 142 cm^{-1} was observed. On the basis of a previous report by Ishioka and co-workers, [61] this value has been correlated to a bridging bi-dentate co-ordination.

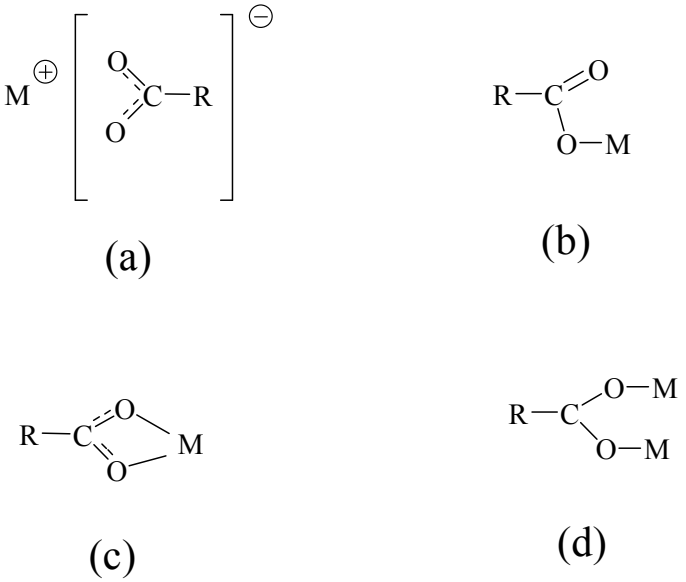

Figure 5. Binding in the carboxylate metal structures is shown; where the structures a-d represents the ionic, uni-dentate, chelating bi-dentate and bridging bi-dentate arrangements respectively.

Trioctylphosphine oxide. Characteristic IR peaks from trioctylphosphine oxide (TOPO) appear at 2954, 2922, 2872 and 2852 cm^{-1} from the alkyl chain. Similar to the ZnSt, these bands have been assigned to the asymmetric and symmetric stretching vibrations of the $-CH_3$ and $-CH_2$ groups (Table I). The peaks at 1464 and 724 cm^{-1} have been assigned to the in-plane and out-of-plane deformation of $-CH_2$ group respectively. Characteristic sharp peak appear at 1146 cm^{-1} that has been assigned to the P=O stretching band. The peak positions were found to be in agreement with the study by McQuillan and co-workers. [41]

ZnS Nanoparticles. The undoped ZnS nanoparticles show characteristic IR peaks between 2955-2845 cm^{-1} from the long alkyl chain, between 1540-1360 cm^{-1} from the carboxylate group, a broad band centered around 1160-1100 cm^{-1} in the P=O IR band region and at 1470-1455, 717 cm^{-1} from the methylene in-plane and out-of-plane deformations respectively. A comparison of the peaks in the ZnS nanoparticles studied with that obtained in pure ZnSt and TOPO reveals some characteristic features. First, the peak positions arising from the $-CH_2$ and $-CH_3$ stretching vibrations in the ZnS nanoparticles were found to be nearly identical with that obtained in either the ZnSt or TOPO. This indicates that the longer alkyl chain is oriented on the nanoparticles in an ordered way. Second, the spectral region involving the carboxyl asymmetric, stretching and methylene in-plane deformation frequency (~1540-1360 cm^{-1}) show multiple peaks. The characteristic IR peaks in the ZnS nanoparticles appear at 1539, 1470-1454 and 1398 cm^{-1} and has been assigned to the ν_{as} [COO^-], δ [CH_2] and ν_s [COO^-] respectively. In addition to this, a peak appears at 1372 cm^{-1} and has also been assigned to ν_s [COO^-] vibration (*vide infra*). From this it is evident that at least a part of the capping on the nanoparticles is by the $-COO^-$ group and there exists co-ordination environments for the carboxylate group that is different compared to that in the pure ZnSt.

Moreover, the in-plane deformation band from the $-CH_2$ group is more structured in the nanoparticles. Third, the spectral region around 1150 cm^{-1} (with the P=O peak from TOPO) has broad features in the nanoparticles and appears in the range of 1160-1100 cm^{-1}. The broad feature argues that there exists multiple co-ordination environments by which the capping of TOPO molecule occurs on the surface of the nanoparticles. Moreover, the absence of sharp peak at 1146 cm^{-1} in the nanoparticles is an indication of the absence of free TOPO molecules.

Overall, the IR spectra acquired with the ZnS nanoparticles identifies both stearate and TOPO as the capping ligand on the surface of the nanoparticles, with capping by the $-COO^-$ and P=O groups on the surface of the nanoparticles and the long chain alkyl group oriented in an ordered crystalline arrangement located away from the nanoparticle.

Zn(Ln)S [Ln=Sm, Eu, Tb, Dy] Nanoparticles. The lanthanide incorporated nanoparticles show characteristic IR peaks between 2955-2845 cm^{-1} from the long alkyl chain, between 1545-1360 cm^{-1} from the carboxylate group, around 1170-1100 cm^{-1} in the P=O IR band region and at 1470-1455, 720 cm^{-1} from the methylene deformations. Similar to the ZnS nanoparticles studied, the spectral region in the carboxylate and P=O IR absorption region indicate that both the stearate and TOPO act as the capping ligand on the lanthanide incorporated ZnS nanoparticles. However, some noticeable differences are obvious between the IR spectra of ZnS and Zn(Ln)S [Ln=Sm, Eu, Tb, Dy] nanoparticles. It appears that the $-COO^-$ stretching bands have been diminished in intensity in the lanthanide incorporated nanoparticles compared to its undoped counterpart. Moreover, the peak at 1370 cm^{-1} is relatively more intense in the Zn(Ln)S compared to that in the ZnS nanoparticles. The assignment of the 1370 cm^{-1} peak originated from the ν_s [COO^-] vibration is based on the consideration of the relative peak intensities of free TOPO molecule. That is, if the 1370

cm^{-1} peak in the Zn(Ln)S nanoparticles has originated from TOPO, the intensity of this peak should be much lower. Based on this, the peaks at ~1400 and ~1370 cm^{-1} in the nanoparticles have both been assigned to the ν_s [COO^-] vibration. This indicates that there exist at least two Δ values for the carboxylate binding, ~140 and 170 cm^{-1} respectively. The higher Δ value points towards a change in the carboxylate binding in the nanoparticles, presumably a change from bridging bi-dentate in the pure ZnSt towards a uni-dentate co-ordination in the Zn(Ln)S nanoparticles. In short, the lanthanide cations are modulating the surface reorganization in the nanoparticles. The extent of surface modulation was found to be nearly independent of the Ln^{3+} [Ln=Sm, Eu, Tb, Dy] identity.

Table I. Position of the IR Peak Frequencies and Corresponding Assignment in the Different Systems Studied.[a]

System	Peak Position (cm^{-1}) and Assignment			
	~3000-2800 cm^{-1}	**~1600-1200 cm^{-1}**	**~1150 cm^{-1}**	**~1000-700 cm^{-1}**
ZnSt	2954 [sh] ν_{as} [CH_3] 2916 [s] ν_{as} [CH_2] 2872 [sh] ν_s [CH_3] 2848 [s] ν_s [CH_2]	1588 [sh] 1538 [s] ν_{as} [COO^-] 1464 [s] δ [CH_2] 1396 [s] ν_s [COO^-] 1324 [m]	----	744 [s] 720 [s] γ [CH_2]
TOPO	2954 [s] ν_{as} [CH_3] 2922 [s] ν_{as} [CH_2] 2872 [sh] ν_s [CH_3] 2852 [s] ν_s [CH_2]	1464 [s] δ [CH_2] 1414 [m] 1376 [m] δ_s [CH_3] 1288 [w] 1242 [m] 1200 [m] δ [CH_2]	1146 [s] ν [P=O] 1118 [sh]	1006 [m] 852 [m] 820 [m] 778 [m] 756 [m] 724 [m] γ [CH_2]
ZnS	2953 [sh] ν_{as} [CH_3] 2916 [s] ν_{as} [CH_2] 2870 [sh] ν_s [CH_3]	1539 [s] ν_{as} [COO^-] 1470 [s] δ [CH_2] 1454 [sh] δ [CH_2]	1160-1100 [br] ν [P=O]	744 [m] 717 [s] γ [CH_2]

	2848 [s] ν_s [CH_2]	1398 [s] ν_s [COO^-] 1372 [vw] ν_s [COO^-]		
Zn(Sm)S	2958 [sh] ν_{as} [CH_3] 2917 [s] ν_{as} [CH_2] 2872 [sh] ν_s [CH_3] 2850 [s] ν_s [CH_2]	1540 [w] ν_{as} [COO^-] 1470 [s] δ [CH_2] 1454 [sh] δ [CH_2] 1401 [w] ν_s [COO^-] 1371 [w] ν_s [COO^-]	1160-1110 [br] ν [P=O]	717 [s] γ [CH_2]
Zn(Eu)S	2956 [sh] ν_{as} [CH_3] 2917 [s] ν_{as} [CH_2] 2871 [sh] ν_s [CH_3] 2848 [s] ν_s [CH_2]	1541 [w] ν_{as} [COO^-] 1470 [s] δ [CH_2] 1457 [sh] δ [CH_2] 1410 [w] ν_s [COO^-] 1371 [w] ν_s [COO^-]	1170-1110 [br] ν [P=O]	717 [s] γ [CH_2]
Zn(Tb)S	2954 [sh] ν_{as} [CH_3] 2916 [s] ν_{as} [CH_2] 2870 [sh] ν_s [CH_3] 2849 [s] ν_s [CH_2]	1542 [w] ν_{as} [COO^-] 1470 [s] δ [CH_2] 1456 [sh] δ [CH_2] 1402 [w] ν_s [COO^-] 1371 [w] ν_s [COO^-]	1170-1110 [br] ν [P=O]	717 [s] γ [CH_2]
Zn(Dy)S	2955 [sh] ν_{as} [CH_3] 2917 [s] ν_{as} [CH_2] 2870 [sh] ν_s [CH_3] 2850 [s] ν_s [CH_2]	1539 [m] ν_{as} [COO^-] 1470 [s] δ [CH_2] 1456 [sh] δ [CH_2] 1401 [w] ν_s [COO^-] 1372 [w-m] ν_s [COO^-]	1170-1110 [br] ν [P=O]	717 [s] γ [CH_2]
ZnSe	2955 [sh] ν_{as} [CH_3] 2917 [s] ν_{as} [CH_2] 2870 [sh] ν_s [CH_3] 2849 [s] ν_s [CH_2]	1541 [m] ν_{as} [COO^-] 1470 [s] δ [CH_2] 1452 [sh] δ [CH_2] 1400 [w] ν_s [COO^-] 1372 [m] ν_s [COO^-]	1158 [m] ν [P=O] 1125 [w]	719 [s] γ [CH_2]
Zn(Tb)Se	2954 [sh] ν_{as} [CH_3]	1540 [w-m] ν_{as} [COO^-]	1160 [s] ν [P=O]	719 [s] γ [CH_2]

	2917 [s] ν_{as} [CH_2] 2872 [sh] ν_s [CH_3] 2850 [s] ν_s [CH_2]	1470 [s] δ [CH_2] 1454 [sh] δ [CH_2] 1410 [w] ν_s [COO^-] 1372 [m] ν_s [COO^-]	1125 [sh]	

[a] The symbols ν, δ and γ refer to stretching, in-plane deformation and out of plane deformation respectively. The symbols s, m, w and sh refer to strong, medium, weak and shoulder respectively.

The IR spectra obtained from the different systems studied were used to compute a parameter (R_1 and R_2) that is a gauge for integrated intensity (in absorbance units) of the capping ligands (stearate and TOPO) with respect to that of the long alkyl chain in a given system (equations 3 and 4).

$$R_1 = \frac{\int I\,[COO^-]\ (\text{asym. str.}) + \int I\,[COO^-]\ (\text{sym. str.})}{\int I\,[CH_2]\ (\text{asym. str.}) + \int I\,[CH_2]\ (\text{sym. str.}) + \int I\,[CH_3]\ (\text{asym. str.}) + \int I\,[CH_3]\ (\text{sym. str.})} \quad (3)$$

$$R_2 = \frac{\int I\,[P{=}O]\ (\text{str.})}{\int I\,[CH_2]\ (\text{asym. str.}) + \int I\,[CH_2]\ (\text{sym. str.}) + \int I\,[CH_3]\ (\text{asym. str.}) + \int I\,[CH_3]\ (\text{sym. str.})} \quad (4)$$

The R_1 and R_2 values provide a measure of the extent of IR absorption of a particular capping ligand (stearate or TOPO) that is normalized to the absorption contribution of the long alkyl chain stretching vibrations from both the capping ligands (stearate and TOPO). Results obtained from this analysis have been summarized in Table IIA. The R_1 and R_2 values decrease in the order ZnSt, TOPO > ZnS, Zn(Ln)S nanoparticles. The values imply a decrease of absorption of the capping ligand with respect to that of the long alkyl chain in the ZnS nanoparticles by at least five times in comparison to the pure ZnSt and TOPO compounds. Presence of lanthanide cations in the Zn(Ln)S nanoparticles further reduces the R_1 value by approximately ten times, in comparison to the undoped ZnS nanoparticles. The reduction in the R_1 and R_2 values suggest a decrease in molar extinction co-efficient of the capping ligands in the Zn(Ln)S nanoparticles (assuming same stiochiometry in pure compound and bound state in the nanoparticles, the intra sample concentration has been taken care of in the denominator of equations 3 and 4 and the pathlength being similar among

different systems). In contrast, the R_2 value in the Zn(Ln)S is of similar magnitude or are slightly higher as compared to that in the undoped ZnS nanoparticles, which imply an increased absorption by the TOPO in comparison to the stearate moiety in the Zn(Ln)S nanoparticles. This is also evident considering the ratio of R_1/R_2. While the R_1/R_2 value is approximately 10 in the undoped ZnS nanoparticles, the corresponding value is in between 0.5-1 in the Zn(Ln)S nanoparticles. This trend suggests a switchover of surface capping properties in the ZnS and Zn(Ln)S nanoparticles studied, that is, while stearate absorption is more predominant in the ZnS nanoparticles as compared to that by TOPO molecules, the situation is reversed in the Zn(Ln)S nanoparticles.

At this point, in the high frequency region of the IR spectra originating from the long alkyl chain, the peak position and the spectral line shape of the strong absorption bands from the $-CH_2$ symmetric and asymmetric stretching frequencies at around 2850 cm^{-1} and 2920 cm^{-1} respectively needs an attention. These peak positions shift to 6 cm^{-1} and 8 cm^{-1} towards higher energy in the liquid state compared to the corresponding crystalline state. Snyder and co-workers [56, 57] have investigated the ratio of peak intensity and integrated intensity of the methylene symmetric and asymmetric stretching bands in this spectral region. Porter, Siperko and co-workers [58] have compared the full width at half maximum (FWHM) in analyzing these bands in the IR spectra. In the present study, an analysis of the spectral line shape in various forms (intensity ratio, integrated intensity ratio, FWHM) have been undertaken for the various systems studied and the results from this analysis have been presented in Table IIB. The analysis reveals the following; (i) the peak intensity ratio and the integrated intensity ratio values were found to be within <15% of standard deviation in the various systems, (ii) the FWHM values of the two bands resemble very close to the corresponding values found in either of the capping ligand (stearate and TOPO) moieties and (iii) there is no obvious dependence due to the presence of the Ln^{3+} cations, as compared to

that in the ZnS nanoparticles. This analysis suggests that in the Zn(Ln)S nanoparticles studied, possible intercalation of Ln^{3+} in the long alkyl chain is not of significant contribution and correspondingly the observed tuning in the IR absorption of the capping ligand moieties has been originated from the Ln^{3+} located on or near the surface of the nanoparticles that are in close proximity to the binding site of the capping ligand moieties.

Table IIA. Comparison of Relative Intensity of Capping Ligand in the Different Systems Studied.[a]

System	R_1	R_2
ZnSt	0.68 ± 0.02	----
TOPO	----	0.097 ± 0.002
ZnS	0.13 ± 0.02	0.013 ± 0.003
Zn(Sm)S	0.014 ± 0.002	0.012 ± 0.002
Zn(Eu)S	0.013 ± 0.001	0.025 ± 0.005
Zn(Tb)S	0.014 ± 0.002	0.029 ± 0.001
Zn(Dy)S	0.016 ± 0.003	0.023 ± 0.003
ZnSe	0.018 ± 0.003	0.020 ± 0.003
Zn(Tb)Se	0.013 ± 0.001	0.057 ± 0.018

[a] For ZnSt, TOPO, ZnS and Zn(Ln)S systems, mean and standard deviation values were reported from three independent measurements. For ZnSe and Zn(Tb)Se systems, the corresponding values were reported from duplicate measurements.

Table IIB. Comparison of IR Spectral Properties in the Methylene Stretching Region in the Different Systems Studied.[a]

System	**I [**ν_{as} $[CH_2]$**] / I [**ν_s $[CH_2]$**]**	**∫I [**ν_{as} $[CH_2]$**] / ∫I [**ν_s $[CH_2]$**]**	**FWHM [**ν_{as} $[CH_2]$**]**	**FWHM [**ν_s $[CH_2]$**]**
ZnSt	1.21 ± 0.08	1.91 ± 0.10	19 ± 1	13 ± 1
TOPO	1.57 ± 0.14	2.31 ± 0.11	26 ± 1	18 ± 1
ZnS	1.28 ± 0.02	2.20 ± 0.03	25 ± 1	14 ± 1
Zn(Sm)S	1.23 ± 0.01	2.18 ± 0.06	26 ± 1	15 ± 1
Zn(Eu)S	1.20 ± 0.08	2.01 ± 0.18	29 ± 3	15 ± 1
Zn(Tb)S	1.29 ± 0.01	2.24 ± 0.15	26 ± 1	14 ± 1
Zn(Dy)S	1.18 ± 0.05	2.18 ± 0.10	28 ± 1	16 ± 1
ZnSe	1.30 ± 0.04	2.43 ± 0.05	25 ± 1	15 ± 1
Zn(Tb)Se	1.23 ± 0.07	2.23 ± 0.04	26 ± 1	15 ± 1

[a] For ZnSt, TOPO, ZnS and Zn(Ln)S systems, mean and standard deviation values were reported from three independent measurements. For ZnSe and Zn(Tb)Se systems, the corresponding values were reported from duplicate measurements.

ZnSe, Zn(Tb)Se Nanoparticles. In order to evaluate the effect of the constituent anion in the vibrational characteristics of the capping ligand in the nanoparticles, experiments were performed with the ZnSe and Zn(Tb)Se nanoparticles. The results have been compared to that obtained in the ZnS and Zn(Ln)S [Ln=Sm, Eu, Tb, Dy] nanoparticles discussed above. Figure 6 represents the FTIR spectra of the ZnSe and Zn(Tb)Se nanoparticles, enlarged in the surface capping ligand (stearate and TOPO) moiety only. Corresponding peak frequencies are summarized in table I. Similar to the ZnS nanoparticles, the signal from the stearate moiety is attenuated in the Tb^{3+} incorporated nanoparticles as compared to that in the undoped system. However, the relative intensity lowering of the stearate asymmetric and symmetric stretching frequencies as compared to that in the pure ZnSt compound is more pronounced in the undoped ZnSe as compared to that in the undoped ZnS nanoparticles. The spectral region consisting of P=O frequency originating from the TOPO moiety show remarkable differences between the ZnSe and ZnS nanoparticles studied. While in the ZnS nanoparticles, a broad signal has been observed; the corresponding signal in the ZnSe nanoparticles show relatively sharper band that is shifted to higher energy with respect to that in the pure TOPO compound. To summarize, a comparison of the results obtained with the undoped and lanthanide incorporated ZnS and ZnSe nanoparticles indicate an (i) attenuation of the stearate IR signal in the doped nanoparticles as compared to that in the undoped system and (ii) enhanced contribution of TOPO absorption (as compared to stearate absorption) in the doped system. However, intrinsic differences between the ZnS and ZnSe nanoparticles studied were evident, as judged by the spectral shape (figures 4 and 6) and relative intensities of different bands (table IIA).

A plausible reason for the difference in the IR absorption characteristics of the TOPO moiety in the ZnS and ZnSe based nanoparticles lies on the smaller difference between the electronegativity and size between oxygen and sulfur as compared to that with oxygen and

selenium. This indicates a greater extent of interaction between the surface localized sulfur atoms in the ZnS based nanoparticles with the P=O moiety of the TOPO molecules. The broad P=O stretching band in the ZnS based nanoparticles has been attributed to the wider variation of interaction between the oxygen and sulfur atoms. On the contrary, the corresponding band in the ZnSe based nanoparticles has been observed as a sharp band that is shifted to higher energy compared to that observed in the free TOPO molecule. The larger extent of difference in electronegativity and size of oxygen and selenium most likely restricts the broader range of interaction between these two atoms. The shift of the P=O stretching band towards higher energy has been attributed to the confinement of the bond in the nanoparticles, which leads to the rigidity of the P=O bond. The FWHM values of the P=O IR stretching band are 20 ± 1 cm^{-1}, 13 ± 2 cm^{-1} and 12 ± 2 cm^{-1} in the TOPO, ZnSe and Zn(Tb)Se nanoparticles respectively, this is consistent with the confined interaction in the ZnSe based nanoparticles compared to the free TOPO molecule.

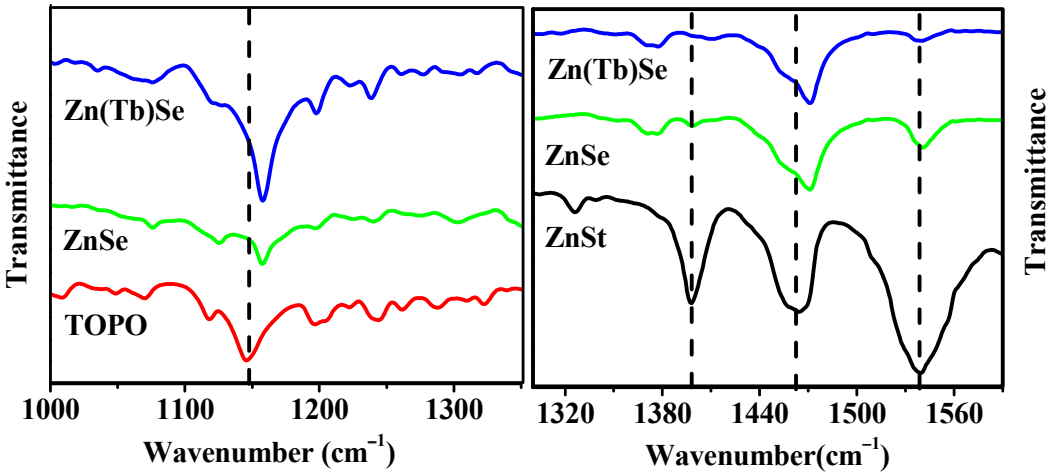

Figure 6. An enlarged view of the FTIR spectra in the P=O (left panel) and the $-COO^-$ (right panel) stretching band regions respectively in the ZnSe based nanoparticles studied is shown. For comparison, corresponding spectra of pure ZnSt and TOPO are included.

At this point, it is worth summarizing the major outcomes from the IR absorption studies from various systems studied. The IR absorption features observed in different systems studied show resemblance and differences in the various spectral regions of interest. The nature of the stretching bands originating from the long alkyl chain in all the nanoparticles studied were found to be similar to that observed in the pure ZnSt and TOPO (both acting as capping ligands in the nanoparticles; *vide supra*) molecules. A noticeable difference in the IR absorption feature was observed in the nanoparticles for the carboxylate and the phosphine oxide stretching bands. While prominent characteristic sharp peak features were evident in the pure ZnSt and TOPO molecules, the ZnS nanoparticles show somewhat reduced carboxylate stretching bands, which has been further reduced in intensity significantly in the Zn(Ln)S [Ln=Sm, Eu, Tb, Dy] nanoparticles studied (Table IIA). On the other hand, the stretching band originating from the phosphine oxide moiety of the TOPO show a broad signature in both the ZnS and Zn(Ln)S [Ln=Sm, Eu, Tb, Dy] nanoparticles, which is in contrast to the sharp P=O absorption observed in the pure TOPO molecule. The absorption contribution of TOPO in the Zn(Ln)S nanoparticles is however higher compared to that in the undoped ZnS nanoparticles (Table IIA). The ZnSe based nanoparticles studied show similar features for the carboxylate stretching bands as compared to that observed in the ZnS based nanoparticles studied, whereas the IR absorption from the TOPO moiety has been observed as a sharp band that is shifted to higher energy as compared to that in the pure TOPO molecule and is in contrast to the broad signature observed from the ZnS based nanoparticles systems studied. At this point, it is to note that none of the nanoparticles studied show IR absorption bands from nitrate groups (typical nitrate bands originate at 1042 and 1335 cm^{-1}) and double bonded carbon atoms at 1642 cm^{-1} that may originate from the octadecene moiety. A similar direct comparison cannot be made for tetracosane, due to its structural feature and the presence of long alkyl chain in both the ZnSt and TOPO molecules.

However, the absence of IR absorption bands of nitrate, double bonded carbon atoms and sharp TOPO signature at 1146 cm^{-1} (*vide supra*) indicate that the nanoparticles used to perform the IR experiments were free from the un-reacted lanthanide cation precursor, octadecene (solvent) and free TOPO molecules.

The IR absorption data presented indicates that the corresponding properties of the capping ligands (stearate and TOPO) can be modulated by the presence of the Ln^{3+} that are located near or on the surface of the Zn(Ln)S [Ln=Sm, Eu, Tb, Dy] nanoparticles. However, these data cannot identify whether the observed tuning of the vibrational characteristics have originated from all or partial population of surface localized Ln^{3+} in the Zn(Ln)S nanoparticles. Stern-Volmer quenching experiment has been undertaken to address this aspect using methanol as a quencher for the Tb^{3+} luminescence. The results obtained from the Stern-Volmer experiment has been summarized in Figure 7a. This analysis assumes that methanol can effectively quench the surface localized Tb^{3+} in the Zn(Tb)S nanoparticles and the quenching process would be less efficient for the Tb^{3+} that are localized at or towards the core of the nanoparticles. A single luminophore population would lead to a single straight line slope with an intercept of unity in a Stern-Volmer plot; any deviation from this with an inclination towards the abscissa could correlate to multiple luminophore population and fractional accessibility of the luminophore to the quencher. Experimentally a deviation from a single slope has been observed indeed. This has been correlated with multiple Tb^{3+} population in the Zn(Tb)S nanoparticles. Specifically, while the initial relatively steeper slope could originate from the surface localized Tb^{3+} in the nanoparticles, there is indeed a population of Tb^{3+} present in the nanoparticles that are better protected from the accessibility of methanol and presumably indicate a core localized lanthanide population. A gradient of lanthanide population from the surface towards the core of the nanoparticles may also be a likely possibility. To summarize, the Stern-Volmer quenching experiment clearly indicate

that all the Tb^{3+} in the Zn(Tb)S nanoparticles are not surface localized. Representative luminescence excitation and emission spectra of the Zn(Tb)S nanoparticles are shown in Figure 7b. The comparison of the Zn(Tb)S spectra in chloroform obtained without and with the addition of 400 µl of methanol indicates that the presence of methanol does not affect the general emission feature of the nanoparticles. Monitoring the emission at 545 nm, the excitation spectra reveal a broad profile without significant contribution from intra-configurational sharp 4f-4f direct excitation bands and the observed excitation profile share common excitation pathway that has been obtained monitoring the nanoparticle emission at 400 nm. This argues in favor of nanoparticle acting as an optical antenna to sensitize the Tb^{3+} luminescence in the samples studied, at least partially.

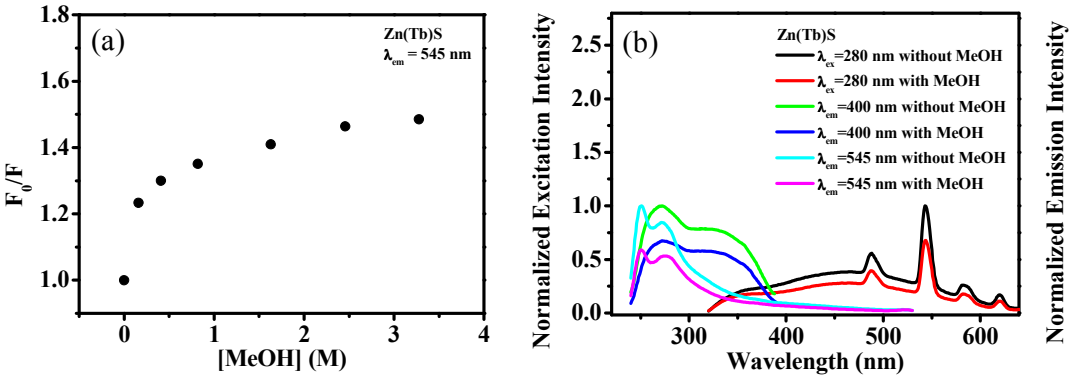

Figure 7. Stern-Volmer plot of Zn(Tb)S nanoparticles using methanol as a quencher is shown in panel (a). The deviation from single straight line slope indicates multiple Tb^{3+} population in the Zn(Tb)S nanoparticles. Representative luminescence excitation and emission spectra of the Zn(Tb)S nanoparticles are shown in panel (b). These spectra indicate that the general luminescence properties of the nanoparticles are not affected by the addition of methanol. The excitation spectra argue in favor of an optical antenna effect to sensitize the Tb^{3+} luminescence. The hump at ~350 nm in the emission spectra has originated from a background contribution in the experiment.

In order to evaluate the possible contribution from the formation of Ln(III) stearate salt and the corresponding dependence from this on the observed IR absorption characteristics in the Zn(Ln)S nanoparticles studied, control experiment has been undertaken

to synthesize Sm(III) stearate and Dy(III) stearate (Sm and Dy have been considered as representative lanthanides) and the IR spectra have been recorded and compared to that obtained with stearic acid and the corresponding Zn(Ln)S nanoparticles studied. The FTIR spectra obtained from this analysis have been summarized in Figure 8. The spectrum from stearic acid show characteristic IR absorption bands at 1702 cm^{-1} and 1296 cm^{-1} respectively that originate from the C=O and C–O stretching bands of carboxylic acids. These bands disappear and new bands originate from the carboxylate asymmetric and symmetric stretching vibrations that appear at 1530-1540 cm^{-1} and 1405-1410 cm^{-1} respectively in the stearate salts, confirming the formation of the salt. These band positions are in reasonable agreement with the corresponding values reported by Binnemans and co-workers for Ln(III) alkanoates. [65, 66] The spectra of the Ln(III) stearate salts clearly deviate from the corresponding Zn(Ln)S nanoparticles and argues that the observed Ln^{3+} induced effect in the Zn(Ln)S nanoparticles is not a mere reflection of the formation of Ln(III) stearate on the surface of the nanoparticles.

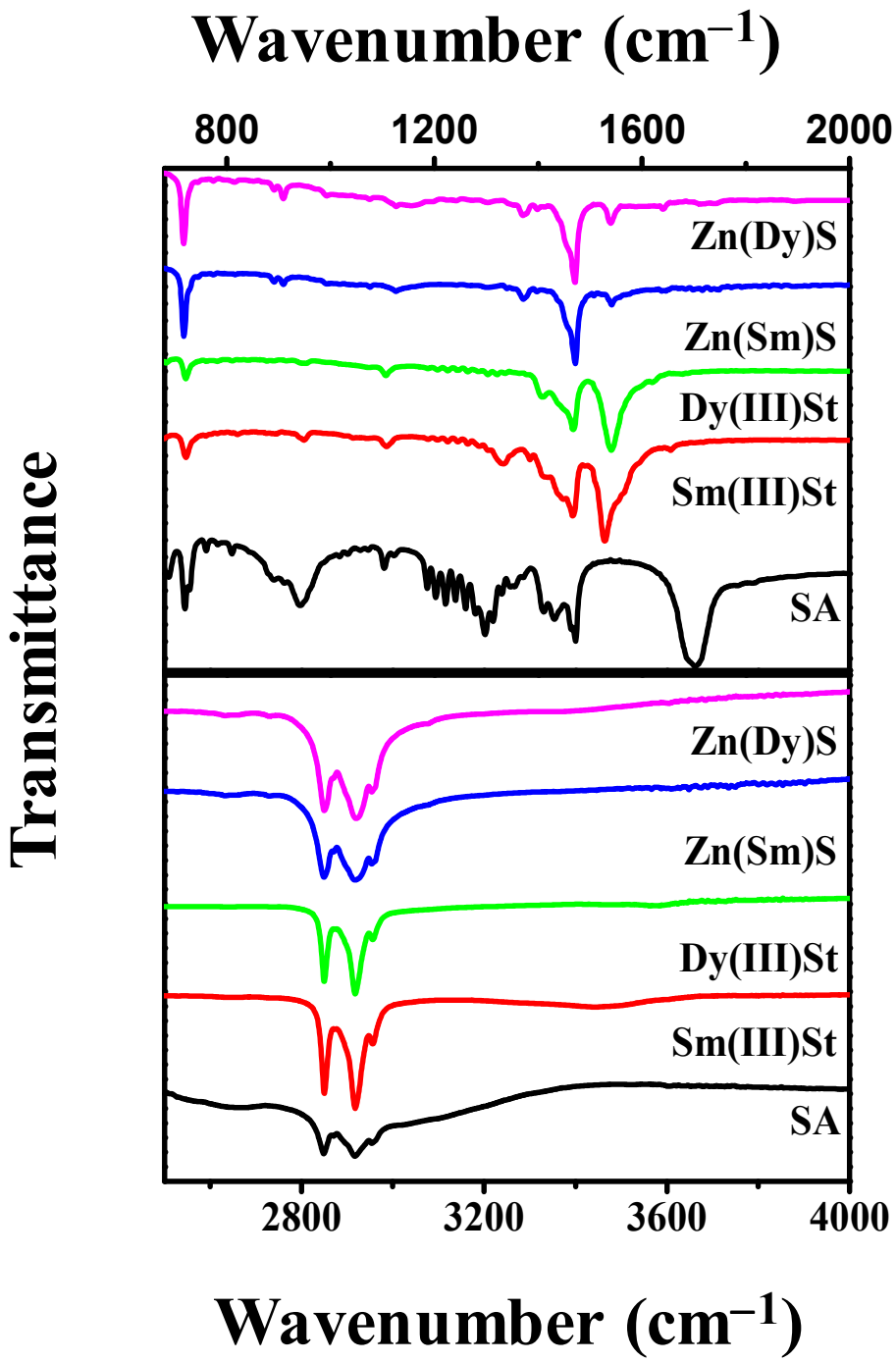

Figure 8. Representative FTIR spectra of stearic acid (SA), Sm(III) stearate, Dy(III) stearate and the corresponding Zn(Ln)S [Ln= Sm, Dy] nanoparticles are shown. The spectra of the Zn(Ln)S [Ln=Sm, Dy] nanoparticles have been included for comparison. The spectra of the lanthanide stearate salts clearly deviate from the corresponding Zn(Ln)S spectra.

Understanding the Ln^{3+} induced tuning of the surface chemistry of nanoparticles may shed light in better understanding the luminescence properties of the lanthanide incorporated

semiconductor nanoparticles. Surface capping ligand induced tuning of nanoparticle luminescence is known. [67-70] For example, for similar sized CdTe nanoparticles capped with 3-Mercaptopropionic acid (MPA) (first excitonic absorption peak maximum at 579 nm) and N,N-dimethyl-2-aminoethanethiol hydrochloride (DEA) (first excitonic absorption peak maximum at 575 nm), the photoluminescence peak maximum has been reported to be 28 nm red shifted in the MPA-CdTe compared to that in the DEA-CdTe nanoparticles. [67] CdSe nanoparticles capped with octadecylphosphonic acid (ODPA), pyridine and aniline as capping ligands show remarkable difference in luminescence efficiency. [70] While the ODPA-CdSe has been found to be strongly luminescent, an emission quenching has been observed in the pyridine-CdSe and the aniline-CdSe was found to have intermediate luminescence among the three systems studied. Sapra and co-workers have reported the role of surface atoms in determining the extent of luminescence in CdSe-CdS and CdSe-ZnS core-shell nanoparticles. [71] While a cation rich surface composition results higher luminescence, an anion rich surface has detrimental effect on the emission intensity. These researchers further demonstrated that the surface composition has a role in deciding the crystal structure (zinc blende or wurtzite) of cadmium chalcogenide nanocrystals. [72] An anion rich surface crystallizes in the zinc blende structure, on the other hand a cation rich surface tends to favour the wurtzite structure. In the context of biological applications of semiconductor nanoparticles, Yamamoto and co-workers [73] have demonstrated that the physicochemical properties and cytotoxicity depends on the nature of the surface molecule that is functionalized in the surface of the nanoparticles. Iyer and co-workers [74] have discussed the role of charge and ligand length on the quantum dots in determining the bio-impact. These studies clearly demonstrate the importance of understanding the surface ligand capping characteristics in semiconductor nanoparticles.

Conclusion

Lanthanide cation (Ln^{3+}) [Ln=Sm, Eu, Tb, Dy] induced changes of the surface capping properties in the Zn(Ln)S nanoparticles have been reported in the present study. The small size (<5 nm in diameter) of the nanoparticles imposes the importance to understand the surface capping properties of the nanoparticles. FTIR spectroscopy revealed the surface capping properties in the nanoparticles and a semi-quantitative analysis from the corresponding IR spectra has been performed in order to gain insight on the relative absorption of the capping ligands. All of the nanoparticles were found to be capped by both the stearate and TOPO moiety with multiple co-ordination environments. A five times reduction of absorbance of the capping ligand with respect to that of the long chain alkyl group has been observed in the undoped ZnS nanoparticles as compared to the pure ZnSt and TOPO molecules. Lanthanide cation incorporation further induces a change in the corresponding absorbance of the capping ligand moieties as compared to that in the undoped ZnS nanoparticles, with a decrease and increase in the stearate and TOPO absorption contribution respectively. The Ln(III) cation induced tuning of the capping ligand IR absorption characteristics has been argued to originate from the lanthanide cations that are located on or near the surface of the Zn(Ln)S nanoparticles. Monitoring the carboxylate asymmetric and symmetric peak frequencies suggests a change in the carboxylate co-ordination from bridging bi-dentate in pure zinc stearate molecule towards a uni-dentate environment in the nanoparticles. The experiments in ZnSe based nanoparticles evaluate the effect of the constituent anion in the nanoparticles. A decrease in absorbance of the stearate capping moiety and an increase in absorbance of the TOPO capping moiety in the Zn(Tb)Se as compared to that obtained in the ZnSe nanoparticles has been observed. These findings are consistent with that found in the ZnS and Zn(Ln)S systems studied. However, intrinsic differences are obvious between the ZnS and ZnSe based nanoparticles, as judged by the

spectral shape and relative intensities of different bands. While the observed differences might be associated to the difference in electronegativity and size between the sulfur and selenium atoms, the underlying mechanism of surface reconstruction in the ZnS and ZnSe nanoparticles and the corresponding modulation upon Ln^{3+} incorporation requires further understanding. The lanthanide cation induced changes in the surface chemistry of nanoparticles might have an impact on the luminescence of the nanoparticles and help guide developing lanthanide incorporated nanoparticles in which the surface properties may be exploited for specific applications.

Acknowledgement

Financial support from the Centre for Research in Nanoscience and Nanotechnology (CRNN), University of Calcutta and the Department of Science and Technology (DST) has been acknowledged. Dr. Ankita Ghatak and Mr. Gouranga H. Debnath acknowledge CRNN for supporting a fellowship. We thank Ms. Urmila Goswami for helping us with the TEM measurements.

References

1. J.-C. G. Bünzli and C. Piguet, *Chem. Soc. Rev.*, 2005, **34**, 1048-1077.
2. S. V. Eliseeva and J.-C. G. Bünzli, *Chem. Soc. Rev.*, 2010, **39**, 189-227.
3. J.-C. G. Bünzli, *Chem. Rev.*, 2010, **110**, 2729-2755.
4. F. S. Richardson, *Chem. Rev.*, 1982, **82**, 541-552.
5. E. G. Moore, A. P. S. Samuel and K. N. Raymond, *Acc. Chem. Res.*, 2009, **42**, 542-552.
6. C. P. Montgomery, B. S. Murray, E. J. New, R. Pal and D. Parker, *Acc. Chem. Res.*, 2009, **42**, 925-937.
7. K. Binnemans, *Chem. Rev.*, **2009**, **109**, 4283-4374.
8. N. Hildebrandt and H.-G. Löhmannsröben, *Curr. Chem. Biol.*, 2007, **1**, 167-186.
9. A. Thibon and V. C. Pierre, *Anal. Bioanal. Chem.*, 2009, **394**, 107-120.
10. F. Wang and X. Liu, *Chem. Soc. Rev.*, 2009, **38**, 976-989.
11. C. Bouzigues, T. Gacoin and A. Alexandrou, *ACS Nano*, 2011, **5**, 8488-8505.
12. J.-C. G. Bünzli and S. V. Eliseeva, *J. Rare Earths*, 2010, **28**, 824-842.
13. W. T. Carnall and P. R. Fields, *Lanthanide/Actinide Chemistry*, American Chemical Society, Washington D. C., 1967.
14. A. Beeby, I. M. Clarkson, R. S. Dickins, S. Faulkner, D. Parker, L. Royle, A. S. deSousa, J. A. G. Williams and M. Woods, *J. Chem. Soc., Perkin Trans. 2*, 1999, 493-503.

15. D. A. Chengelis, A. M. Yingling, P. D. Badger, C. M. Shade and S. Petoud, *J. Am. Chem. Soc.*, 2005, **127**, 16752-16753.
16. P. Mukherjee, C. M. Shade, A. M. Yingling, D. N. Lamont, D. H. Waldeck and S. Petoud, *J. Phys. Chem. A*, 2011, **115**, 4031-4041.
17. H. Uh and S. Petoud, *Comptes Rendus Chimie*, 2010, **13**, 668-680.
18. J. Planelles-Aragó, B. Julián-López, E. Cordoncillo, P. Escribano, F. Pellé, B. Viana and C. Sanchez, *J. Mater. Chem.*, 2008, **18**, 5193-5199.
19. J. Planelles-Arago, E. Cordoncillo, R. A. S. Ferreira, L. D. Carlos and P. Escribano, *J. Mater. Chem.*, 2011, **21**, 1162-1170.
20. C. Xueyuan, L. Wenqin, L. Yongsheng and L. Guokui, *J. Rare Earths*, 2007, **25**, 515-525.
21. J. P. Cross, M. Lauz, P. D. Badger and S. Petoud, *J. Am. Chem. Soc.*, 2004, **126**, 16278-16279.
22. K. A. White, D. A. Chengelis, K. A. Gogick, J. Stehman, N. L. Rosi and S. Petoud, *J. Am. Chem. Soc.*, 2009, **131**, 18069-18071.
23. A. A. Bol, R. v. Beek and A. Meijerink, *Chem. Mater.*, 2002, **14**, 1121-1126.
24. L. Chen, J. Zhang, S. Lu, X. Ren and X. Wang, *Chemical Physics Letters*, 2005, **409**, 144-148.
25. N. Jing-hua, H. Rui-nian, L. Wen-lian, L. Ming-tao and Y. Tian-zhi, *J. Phys. D: Appl. Phys.*, 2006, **39**, 2357-2360.
26. G. Ehrhart, B. Capoen, O. Robbe, F. Beclin, P. Boy, S. Turrell and M. Bouazaoui, *Optical Materials*, 2008, **30**, 1595-1602.
27. L. Dong, Y. Liu, Y. Zhuo and Y. Chu, *Eur. J. Inorg. Chem.*, 2010, 2504-2513.
28. P. Mukherjee, R. F. Sloan, C. M. Shade, D. H. Waldeck and S. Petoud, *J. Phys. Chem. C*, 2013, **117**, 14451-14460.
29. D. H. Son, S. M. Hughes, Y. Yin and A. P. Alivisatos, *Science*, 2004, **306**, 1009-1012.
30. R. D. Robinson, B. Sadtler, D. O. Demchenko, C. K. Erdonmez, L.-W. Wang and A. P. Alivisatos, *Science*, 2007, **317**, 355-358.
31. D. Mocatta, G. Cohen, J. Schattner, O. Millo, E. Rabani and U. Banin, *Science*, 2011, **332**, 77-81.
32. B. J. Beberwyck, Y. Surendranath and A. P. Alivisatos, *J. Phys. Chem. C*, 2013, **117**, 19759-19770.
33. J. B. Rivest and P. K. Jain, *Chem. Soc. Rev.*, 2013, **42**, 89-96.
34. C. Dong and F. C. J. M. vanVeggel, *ACS Nano*, 2009, **3**, 123-130.
35. M. E. Abrishami, A. Kompany, S. M. Hosseini and N. G. Bardar, *J. Sol-Gel Sci. Technol.*, 2012, **62**, 153-159.
36. W. Wang, X. Chen and S. Efrima, *J. Phys. Chem. B*, 1999, **103**, 7238-7246.
37. A. Gupta, C. Schulz and H. Wiggers, *Journal of Optoelectronics and Advanced Materials*, 2010, **12**, 518-522.
38. B. S. Kim, L. Avila, L. E. Brus and I. P. Herman, *Appl. Phys. Lett.*, 2000, **76**, 3715-3717.
39. J. Chen, Q. Meng, P. S. May, M. T. Berry and C. Lin, *J. Phys. Chem. C*, 2013, **117**, 5953-5962.
40. T. Grzyb, M. Runowski, A. Szczeszak and S. Lis, *J. Phys. Chem. C*, 2012, **116**, 17188-17196.
41. A. G. Young, N. Al-Salim, D. P. Green and A. J. McQuillan, *Langmuir*, 2008, **24**, 3841-3849.

42. A. P. Duarte, L. ï. Mauline, M. Gressier, J. Dexpert-Ghys, C. Roques, J. M. A. Caiut, E. Deffune, D. C. G. Maia, I. Z. Carlos, A. A. P. Ferreira, S. J. L. Ribeiro and M.-J. l. Menu, *Langmuir*, 2013, **29**, 5878-5888.
43. T. Posati, F. Costantino, L. Latterini, M. Nocchetti, M. Paolantoni and L. Tarpani, *Inorg. Chem.*, 2012, **51**, 13229-13236.
44. W. W. Yu, Y. A. Wang and X. Peng, *Chem. Mater.*, 2003, **15**, 4300-4308.
45. S.-L. Iconaru, M. Motelica-Heino and D. Predoi, *Journal of Spectroscopy*, 2013, Article ID 284285, 284210 pages.
46. Q. Wang, T. Fang, P. Liu, B. Deng, X. Min and X. Li, *Inorg. Chem.*, 2012, **51**, 9208-9213.
47. X. Wu, D. Wang and S. Yang, *Journal of Colloid and Interface Science*, 2000, **222**, 37-40.
48. W. Xu, B. A. Bony, C. R. Kim, J. S. Baeck, Y. Chang, J. E. Bae, K. S. Chae, T. J. Kim and G. H. Lee, *Nature Scientific Reports*, 2013, **3**, 3210.
49. L. S. Li, N. Pradhan, Y. Wang and X. Peng, *Nano Lett.*, 2004, **4**, 2261-2264.
50. N. Pradhan, D. M. Battaglia, Y. Liu and X. Peng, *Nano Lett.*, 2007, **7**, 312-317.
51. L. E. Brus, *J. Chem. Phys.*, 1984, **80**, 4403-4409.
52. K. Sooklal, B. S. Cullum, S. M. Angel and C. J. Murphy, *J. Phys. Chem.*, 1996, **100**, 4551-4555.
53. S. Sapra, N. Shanthi and D. D. Sarma, *Phys. Rev. B*, 2002, **66**, 205202-205201-205202-205208.
54. R. Viswanatha, S. Sapra, T. Saha-Dasgupta and D. D. Sarma, *Phys. Rev. B*, 2005, **72**, 045333-045331-045333-045310.
55. S. Toda, E. Sakai and Y. Kojima, *Spectrochimica Acta*, 1971, **27A**, 581-592.
56. R. G. Snyder, S. L. Hsu and S. Krimm, *Spectrochimica Acta*, 1978, **34A**, 395-406.
57. R. G. Snyder, H. L. Strauss and C. A. Elllger, *J. Phys. Chem.*, 1982, **86**, 5145-5150.
58. E. L. Smith, C. A. Alves, J. W. Anderegg, M. D. Porter and L. M. Siperko, *Langmuir*, 1992, **8**, 2707-2714.
59. G. B. Deacon and R. J. Phillips, *Coordination Chemistry Reviews*, 1980, **33**, 227-250.
60. T. Ishioka, Y. Shibata, M. Takahashi, I. Kanesaka, Y. Kitagawa and K. T. Nakamura, *Spectrochimica Acta Part A*, 1998, **54**, 1827-1836.
61. T. Ishioka, Y. Shibata, M. Takahashi and I. Kanesaka, *Spectrochimica Acta Part A*, 1998, **54**, 1811-1818.
62. E. G. Palacios, G. Jua´rez-Lo´pez and A. J. Monhemius, *Hydrometallurgy*, 2004, **72**, 139-148.
63. V. Zeleňák, Z. Vargová and K. Györyová, *Spectrochimica Acta Part A*, 2007, **66**, 262-272.
64. S. K. Papageorgiou, E. P. Kouvelos, E. P. Favvas, A. A. Sapalidis, G. E. Romanos and F. K. Katsaros, *Carbohydrate Research*, 2010, **345**, 469-473.
65. K. Binnemans, L. Jongen, C. Bromant, D. Hinz and G. Meyer, *Inorg. Chem.*, 2000, **39**, 5938-5945.
66. L. Jongen, K. Binnemans, D. Hinz and G. Meyer, *Liquid Crystals*, 2001, **28**, 1727-1733.
67. M. Wu, P. Mukherjee, D. N. Lamont and D. H. Waldeck, *J. Phys. Chem. C*, 2010, **114**, 5751-5759.
68. C. Bullen and P. Mulvaney, *Langmuir*, 2006, **22**, 3007-3013.
69. K. E. Knowles, D. B. Tice, E. A. McArthur, G. C. Solomon and E. A. Weiss, *J. Am. Chem. Soc.*, 2010, **132**, 1041-1050.
70. B. P. Bloom, L.-B. Zhao, Y. Wang, D. H. Waldeck, R. Liu, P. Zhang and D. N. Beratan, *J. Phys. Chem. C*, 2013, **117**, 22401-22411.

71. U. Soni and S. Sapra, *J. Phys. Chem. C*, 2010, **114**, 22514-22518.
72. U. Soni, V. Arora and S. Sapra, *CrystEngComm*, 2013, **15**, 5458-5463.
73. A. Hoshino, K. Fujioka, T. Oku, M. Suga, Y. F. Sasaki, T. Ohta, M. Yasuhara, K. Suzuki and K. Yamamoto, *Nano Lett.*, 2004, **4**, 2163-2169.
74. A. Nagy, A. Steinbrück, J. Gao, N. Doggett, J. A. Hollingsworth and R. Iyer, *ACS Nano*, 2012, **6**, 4748-4762.